Wear 558–559 (2024) 205554

Contents lists available at ScienceDirect

Wear

journal homepage: www.elsevier.com/locate/wear

Resolving high-strain-rate scratch behavior of Ti6Al4V in experiment and meshless simulation

A.M. Ventura Cervellón [a,b], M. Varga [a], M. Rodríguez Ripoll [a], S.J. Eder [a,b,*]

[a] AC2T research GmbH, Viktor Kaplan-Straße 2/c, Wiener Neustadt, 2700, Austria
[b] Institute for Engineering Design and Product Development, TU Wien, Lehárgasse 6 – Objekt 7, 1060 Vienna, Austria

ARTICLE INFO

Keywords:
Scratch test
Material point method
Abrasion
Tribology
High strain rate

ABSTRACT

The outstanding strength-to-weight ratio and corrosion resistance of titanium have made it the material of choice in the aerospace industry and medicine. The alpha–beta alloy Ti6Al4V is particularly preferred for its excellent mechanical and bio-compatible properties. Despite its advantages, the low thermal conductivity and poor tribological performance of titanium pose significant challenges during manufacturing and in operation. This research offers deep insights into the high strain rate behavior of Ti6Al4V under abrasive load, such as e.g. experienced in machining, by modifying the standard scratch test setup and using optimized Johnson–Cook material parameters to perform Material Point Method (MPM) simulations. The MPM simulations provide accurate predictions of the data gathered through high strain rate scratch experiments. We found an increase in the von Mises stress distribution as well as the normal and tangential forces required to perform a scratch of the same depth as the strain rate increases. The morphology of the scratch profiles also showed an increase in the height of the ridges that form as the scratching speed increases. These findings are in line with the increase in yield strength and work hardening with growing strain rate. This study bridges the gap between simulation models and experimental observations by providing insights for improved machining strategies and surface treatments that can enhance the performance of Ti6Al4V in demanding applications.

1. Introduction

Titanium, recognized for its impressive strength-to-weight ratio, stands as one of the most sought-after metals in various industries, particularly over the last decade where the publications about titanium had a growth rate of 164.75% between the years 2010 to 2020 [1], as also shown in Fig. A.1 within a diversity of disciplines. Its importance is derived not only from its strength but also from its remarkable resistance to corrosion, as well as its ability to withstand extreme temperatures [2]. This unique combination of mechanical and chemical properties ensures that titanium is not only light but also durable, making it an ideal material choice for diverse applications. In the aerospace industry, it is widely used in aircraft structures and engines for its high strength and low density. In medical applications, because of its bio-compatibility, it is used in surgical instruments and prostheses, and due to its corrosion resistance it has been used extensively in marine applications and in the chemical processing industry. Lastly, in everyday life applications, it finds its place in sports equipment, eyeglass frames, and even jewelry [3].

At low temperatures, pure titanium has hexagonal close packed structure (hcp), called α titanium, while at high temperatures the stable structure is body-centered cubic (bcc), or β titanium, with the β-transus temperature for pure titanium located at 882 ± 2 °C [4]. The combination of these two crystal structures is the base for the large number of alloys and their varying properties [5]. Therefore, titanium alloys are generally classified as: alpha (α), beta (β) and alpha–beta ($\alpha+\beta$). Ti6Al4V or titanium Grade 5 is an $\alpha+\beta$ alloy, which has become the preferred alloy to use particularly in aerospace and biomedical applications due to its high strength-to-weight ratio, low density, bio compatibility and chemical stability [6].

Despite their notable positive attributes, titanium and its alloys are also characterized by their low thermal conductivity. This results in poor machinability, as the retained heat at the point of contact adversely affects the tool. Furthermore, titanium is also known for having poor tribological properties, which significantly impact its performance in applications involving friction and wear. One of the primary issues with titanium is its low shear strength, making it more susceptible to adhesive wear, a type of wear that occurs when material transfers between surfaces in contact due to strong adhesive forces. This tendency toward adhesion is problematic because it can lead to galling, where material from one surface sticks to another, creating rough surfaces and

* Corresponding author at: Institute for Engineering Design and Product Development, TU Wien, Lehárgasse 6 – Objekt 7, 1060 Vienna, Austria.
E-mail address: stefan.eder@ac2t.at (S.J. Eder).

https://doi.org/10.1016/j.wear.2024.205554
Received 18 March 2024; Received in revised form 23 August 2024; Accepted 27 August 2024
Available online 30 August 2024

increasing friction. Consequently, titanium exhibits poor wear resistance, meaning it degrades faster under repeated sliding conditions [2]. The combination of low shear strength and high adhesion propensity can result in high coefficients of friction when titanium is in dry contact with a variety of materials. In dry conditions, where no lubricants are present to reduce friction, the coefficient of friction of titanium is particularly high. This not only makes movement less efficient but also contributes to accelerated wear. As a result, titanium experiences high wear rates, meaning it loses material more quickly when subjected to frictional forces. This is a significant drawback in applications where durability and longevity are critical, as frequent wear events can lead to failure or the need for regular maintenance and replacement [7,8].

Modern machining operates with high-strain-rate deformations of the materials that are being manufactured. Although difficult to assess, the effects of high strain rates on the properties of diverse materials have been investigated experimentally, e.g., in [9,10]. For instance, Yadav and Ramesh [11] made use of the split-Hopkinson bar technique to study tungsten-based composites, finding an increase in flow stress with the increase of strain rate in a range from 10^3 to 10^5 s^{-1}. Chiem and Duffy [12] investigated the behavior of aluminum using a torsional Hopkinson bar setup and found a strong increase in strain rate sensitivity when exceeding 500 s^{-1}. Particularly for Ti6Al4V, Lee [13] made use of the split-Hopkinson pressure bar and found that the flow stress has a strong dependence on strain rate and temperature. It was also found that yield strength increases with strain rate at temperatures from 25 to 1100 °C and that there is a pronounced increase in strain rate sensitivity at high strain rates and high temperatures.

Therefore, a comprehensive understanding of the mechanical properties of Ti6Al4V and its response to high strain rates remains an important area of study and is relevant to efficient machining, study of the wear behavior and long-term reliability of titanium components [14].

While traditional methods of tension, compression, and torsion tests have been employed extensively, their destructive nature and requirement for specific sample geometries have often posed limitations, especially when dealing with finished components, intricate structures, or the investigation of surface and near-surface properties [15]. Hence, the need for non-destructive methodologies is obvious. In this context, scratch testing emerges as a great alternative. It offers the unique capability of examining in detail the mechanical behavior of coatings and thin films without causing large-scale damage [16,17]. Scratch testing is a suitable technique to obtain valuable information about the mechanical properties of materials, including their hardness, adhesion, and wear resistance [18]. One important limitation of scratch tests is that they are typically performed under quasistatic conditions with extremely low scratch speeds. While this may serve to suitably characterize the cracking and adhesion behavior of coatings, it is not suitable for characterizing the behavior of materials during machining processes or single abrasion wear events, as those processes typically involve strain rates that are several orders of magnitude higher than conventional scratch speeds [19].

An adaptation of the well-established scratch test method holds potential for unveiling the surface properties of materials, especially when paired with modern computational tools like the Material Point Method (MPM) [20]. MPM is a particle-based method that offers the implementation of the Generalized Interpolation Material Point Method (GIMP) within the open-source code LAMMPS [21].

The non-destructive character of the scratch test, coupled with the enhanced analytical capabilities of MPM simulations [22], can provide valuable insights into the mechanical and wear behavior of materials [23,24]. Given MPM's distinct capabilities of handling large deformations and material removal, the method can provide important information about the wear and machining behavior of Ti6Al4V. This is especially true for understanding the strain rate dependence, which may pose challenges in conventional test rig setups and may provide only bulk properties [25]. One of the main challenges of scratch tests is the difference in velocity regimes, when it comes to experimental scratches and industrial processes that happen at (severely) higher speeds, especially when the materials have a notable strain rates dependence. However, when it comes to simulations, the limitations regarding scratch speeds are given by the required computational resources. While simulations at high speed are easy to perform, these results cannot be straightforwardly compared to experimental scratches performed in a standard (low-speed) scratch tester. Fig. 1 illustrates these differences in velocity regimes, where simulations and standard scratch tests are separated by orders of magnitude.

Table 1
Chemical composition of the alloy Ti6Al4V in wt.% [31].

C	O	N	H	Fe	Al	V	Others	Ti
≤0.08	≤0.2	≤0.05	≤0.015	≤0.4	5.5–6.75	3.5–4.5	≤0.4	Base

Aside from the MPM simulation technique, scratch test simulations have also been widely explored using the Finite Element Method (FEM) by different authors. Bucaille et al. [26] worked on a three-dimensional model with the use of the software Forge3 with a fixed scratch depth of 3 mm, 10 mm/s scratching speed and frictionless contact to study the response of elastic–plastic materials. Doman et al. [27] worked with an LS-DYNA model for AISI 4340, using fully integrated elements, element erosion controls, and performing an extensive convergence study from which they considered the 10 μm element size as the most adequate in terms of accuracy versus computational time and making use of the well-established Johnson–Cook constitutive material model. Holmberg et al. [28–30] worked on a detailed study of scratch simulations with the Warp3D and ABAQUS software to investigate the behavior of a titanium nitride coating, using a displacement controlled setup, defining the indenter as a rigid body and increasing the load from 5 to 50 N with a maximum scratch depth of 3 μm.

This work aims to build a complementary approach between experimental and simulated scratches with a focus on high strain rates that can provide valuable insights into the mechanical behavior of materials at high speeds. Closing this gap between experiments and simulations has been achieved in this work by modifying the standard scratch test setup and by performing MPM simulations representing the scratch system. Ti6Al4V has served as illustrative example of an alloy with high strain rate dependence. It was chosen as it is an alloy with a wide range of applications ranging from aerospace to biomedical implants and whose behavior during abrasive or erosive events at high strain rates is of high industrial relevance.

2. Material and methods

2.1. Material

The material selected for this work was the α–β titanium alloy Ti6Al4V due to its industrial relevance in a wide range of applications. The tested samples were blocks of approximately 90 × 22 × 10 mm^3. The material is standardized in the ASTM B265 standard [31], and the corresponding chemical composition is shown in Table 1.

2.2. Scratch test

The experimental scratches spanned a wide range of speed regimes: low-speed and high-speed scratches were performed to assess the response of the material at different strain rates.

The low-speed scratches were performed in an automatized standard Scratch-Tester (Millennium 100), which is in accordance with the European Standard EN 1071-3 [34] and the ASTM G171 [35]. It can operate in a range of loads from 0.05 to 100 N and a loading rate range from 30 to 500 N/min. The maximum scratch length is 30 mm, and it features a linear motorized stage with 180 mm travel distance in x, 25 mm in y, and a step of 0.5 mm. The indenter used for the scratches

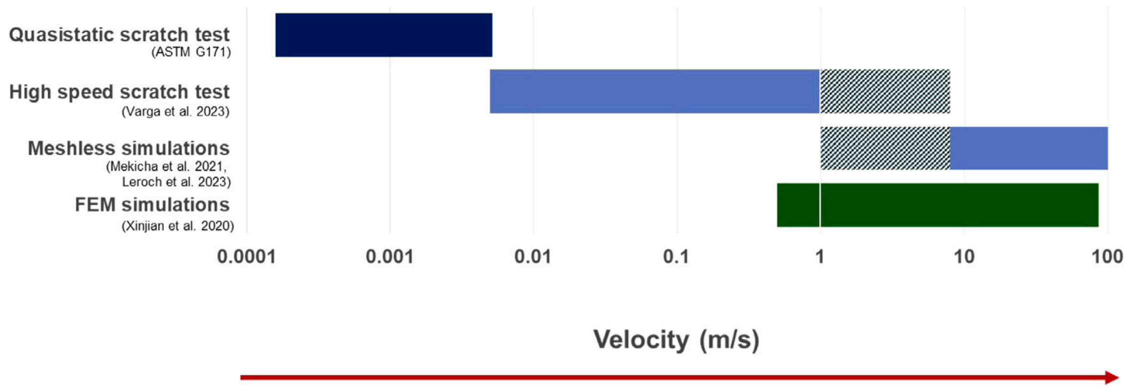

Fig. 1. Velocity ranges in scratch tests: Experimental [20,31] and simulation [24,32,33]. Dark blue corresponds to the range of velocities for standard scratches, light blue to experiments and simulations shown in this work, and green to the range of velocities for FEM simulations not discussed within this work. (For interpretation of the references to color in this figure legend, the reader is referred to the web version of this article.)

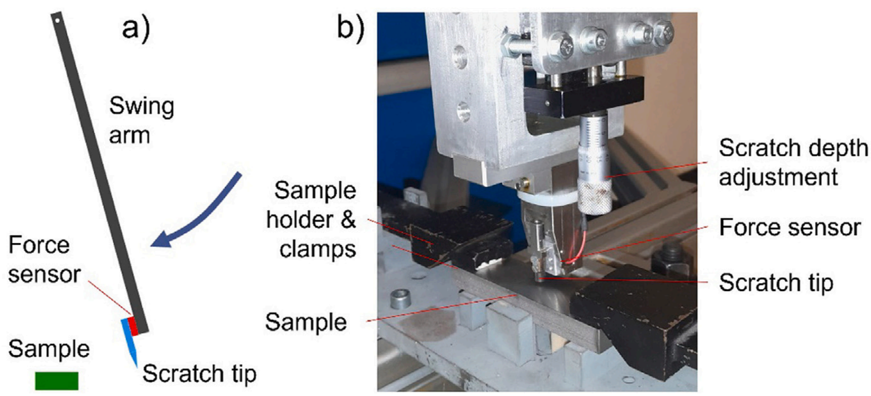

Fig. 2. Experimental set up for the high speed scratches as described by Varga et al. [20]: (a) sketch of working principle of the pendulum-type high-speed scratch tester; (b) detail of contact zone between indenter and sample, clearly visible is the depth adjustment gauge [20].

was a Rockwell C diamond indenter with a tip radius of 200 μm on top of a cone of 120° opening angle.

The scratches on the Ti6Al4V sample were performed at a sliding speed of 5 mm/s, this being the highest speed indicated in the ASTM G171 standard [35] and already significantly higher than the usual operating speed of 10 mm/min (0.167 mm/s). Scratches were performed at different loads: 10, 20, 30, 40 and 50 N to achieve different indentation depths and deformation, respectively, with three repetitions for each load. The length of each scratch was 15 mm.

The high-speed scratches were performed using the in-house designed test rig described in [20] and shown in Fig. 2, which features a pendulum system with a swing arm of ~1 m in length. Due to its dimensions and weight, it should reach a speed of 8 m/s during a scratch, which has proven to actually be around 6.8 m/s in [20]. The used indenter was the same as in the low-speed scratches for best comparison. In this test rig, the samples were placed in the bottom of the setup and fixed with clamps (Fig. 2b).

The scratches were performed one after another by laterally adjusting the position of the pendulum with the aid of a screw system in the top end of the arm. The height of the indenter, and therefore the depth of the scratches, was manually adjusted for each scratch within a range of 10 to 50 μm.

2.3. MPM simulations

The numerical simulations were performed using a meshless technique that can inherently handle large deformations: the Material Point Method (MPM) [36] that provides an implementation of the Generalized Interpolation Material Point Method (GIMP) [37] in the open-source code LAMMPS [21] with the SMD package [38]. The simulated samples had dimensions of $3.0 \times 1.0 \times 0.4$ mm with a particle diameter of 10 μm, producing a system with ~1.2 million particles (after a particle size dependence study discussed in Section 3.1). The indenter used in the simulations represents the tip of the Rockwell C-shaped indenter used in the experiments, a sphere of 200 μm radius defined as a rigid body. The scratch length for all the simulations was limited to 2 mm for computational efficiency, which has proven to be long enough for producing a stable scratch behavior for comparison purposes between experimental and simulated data. The contact between the two surfaces was simplified to a frictionless interaction to optimize the use of computational resources.

Each simulation was divided into two stages: the first stage is an indentation procedure, where the indenter is moved to the desired scratch depth; the second stage is the displacement of the indenter along the x axis for a length of 2 mm. The general setup for the scratch simulations is shown in Fig. 3, and the most relevant simulation parameters are displayed in Table 3.

The material model used in the simulations was the widely used Johnson–Cook viscoplastic material model [39], which is a robust empirical model suitable to model viscoplastic behaving materials such as most metals. In this model, the relation of the von Mises flow stress σ_f is defined as:

$$\sigma_f(\epsilon, \dot{\epsilon}, T) = [\sigma_y + B(\epsilon)^n][1 + C \ \ln \dot{\epsilon}^*][1 - (T^*)^m] \ , \tag{1}$$

where in the first term, which models the strain hardening behavior, σ_y is the material yield stress, B is the strain hardening coefficient, ϵ is the equivalent plastic strain, and n is the strain hardening exponent. In the

Table 2
Johnson–Cook parameters used to model the behavior of Ti6Al4V at high strain rates [33].

Young's modulus E (GPa)	Yield strength σ_y (MPa)	Strain hardening coefficient B	Strain hardening exponent n	Strain rate coefficient C
105	790	478	0.28	0.032

second term, which describes the strain rate sensitivity, C is the strain rate coefficient and $\dot{\epsilon}^*$ is the normalized strain rate, which is given as:

$$\dot{\epsilon}^* = \frac{\dot{\epsilon}}{\dot{\epsilon}_0} , \tag{2}$$

where $\dot{\epsilon}$ is the measured plastic strain rate and $\dot{\epsilon}_0$ is a user-defined reference strain rate. The third term governs the thermal softening response, where m is the temperature exponent and T^* is the normalized temperature defined as:

$$T^* = \frac{T - T_0}{T_m - T_0} , \tag{3}$$

where T_0 is the reference temperature and T_m is the melting temperature of the material.

The values of the different Johnson–Cook parameters for Ti6Al4V are given in Table 2 and were taken from Ref. [33], where they optimized the Ti6Al4V Johnson–Cook parameters for high strains in cutting processes with speeds ranging from 0.05 m/s up to 86.5 m/s, which is comparable to the range investigated in this work. Note that we omitted the final term in the Johnson–Cook model in our analysis. This decision was based on the observation that the thermal effects generated during scratching, even at the highest speed of 100 m/s, would result in a maximum flow stress reduction of only 4% or less.

However, the heat conduction computations that allowed us to assess this influence were performed by enabling the thermal function when defining the particle interactions within the MPM code. The heat distribution is computed directly on the grid using central differences and a three point stencil and is then time-integrated using a forward Euler update. By implementing this, we solve the transport equation

$$\dot{q} = \alpha \nabla^2 q , \tag{4}$$

where q is heat, and α is the thermal diffusion constant, which is calculated from the heat conduction coefficient of the material. The relationship between thermal conductivity and the thermal diffusion constant is given by:

$$\alpha = \frac{\kappa}{\rho \ c_p} , \tag{5}$$

where κ is the thermal conductivity of the given material, ρ its density, and c_p the specific heat. The per-particle-temperature details are then obtained as outlined in Eq. (6).

$$T = \frac{q}{m \ c_p} , \tag{6}$$

making use of the heat, mass and specific heat quantities for the specified material. These parameters are given for Ti6Al4V in Table 3. Some of the observations about temperature increase in the near surface area are shown in Fig. A.2 for the 100 m/s and 6.5 m/s scratches.

Three different sets of simulations were performed within the scope of this investigation:

- *Lattice sensitivity study:* the main goal of these simulations was to investigate the influence of the particle size on the results while considering the computational resource expenditure. For this purpose, the same system was resolved for particle sizes of 5, 7.5, 10, 15, and 20 μm. These simulations were performed at a scratch depth of 20 μm and a scratch speed of 50 m/s. The median profile of each scratch was extracted to assess any differences depending on the particle size. These are discussed in Section 3.1.
- *Scratch depths:* scratches were performed at different depths to assess the response of the material and to compare this behavior with the experimental scratches. For this purpose, scratches of 10, 20, and 25 μm in depth were set up. These simulations were performed using a 10 μm particle size and a speed of 100 m/s.

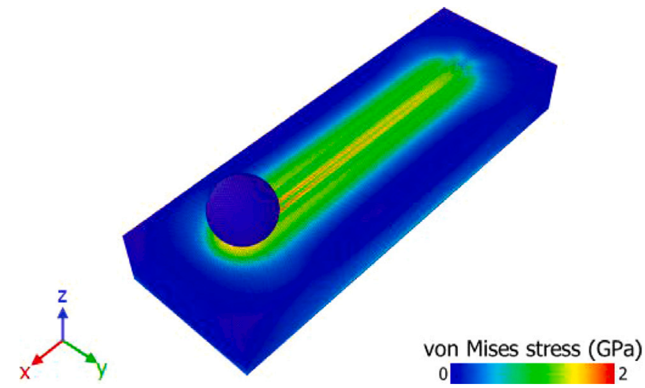

Fig. 3. MPM scratch simulation setup featuring the von Mises stress distribution after the scratch. The scratch was performed along the x axis on a sample of $3.0 \times 1.0 \times 0.4$ mm with a particle size of 10 μm.

Table 3
Relevant simulation parameters.

Sample size (L × W × H)	3 × 1 × 0.4	mm^3
Domain size (L × W × H)	3.2 × 1.2 × 1	mm^3
Scratch length	2	mm
Particle size	5, 7.5, 10, 15, 20	μm
Scratch depth	10, 20, 25	μm
Lattice	Simple cubic	
Pair style	smd/mpm_linear	
Thermal conductivity	Enabled	
Thermal conductivity (κ)	7.4	W/(m K)
Density (ρ)	4430	kg/m^3
Specific heat (c_p)	520	J/(kg K)

- *Scratch velocity:* the velocity of the simulated scratches was varied to have scratches at a speed comparable to the experimental ones, and to assess the influence of the strain rate on the behavior of the material. The scratch velocities were varied over a range from 1 to 100 m/s, with scratching speeds at 100, 50, 10, 6.5, 5, and 1 m/s, where the scratches performed at 6.5 m/s serve as comparison to the experimental scratches performed on the pendulum test rig.

2.4. Data evaluation

Having two main sources of data, experiments and simulations, the post-processing was performed using different suitable tools. From the experimental side, the surface of the scratched samples was further analyzed with topographical measurements and extraction of the median scratch profiles. The results obtained from simulations were post-processed in two stages: visualization and analysis of the output quantities from the simulations.

2.4.1. Topography evaluation

The experimental samples were analyzed by means of topographical measurements making use of the *Alicona® Infinite Focus G5 system*. Once the topography of the scratches were measured, more detailed information is captured from the central section of the scratch where the scratch process is steady and has a constant depth, which was 2 mm for the high-speed scratches and 5 mm for the low-speed experiments. This section of the scratch is used to extract a median profile that is used for comparison purposes between different scratches. These

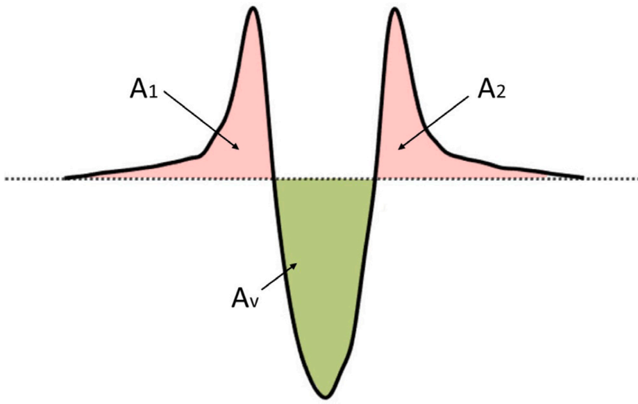

Fig. 4. Definition of the abrasive wear factor f_{ab} according to Zum Gahr [42].

measurements were done on all experimental scratches for both speed regimes: low- and high-speed scratches.

2.4.2. Simulation visualization

The visualization of the simulation results was performed in *OVITO - Version 2.9.0*, which is a scientific visualization and analysis tool designed for models of molecular and other particle-based simulations [40]. From the quantities computed during the simulation, our particular interest was in the von Mises stress distribution, which provides insightful and detailed information about the material response during and after the scratch process (residual stresses). Views with sections in the y-z and x-z planes were generated to observe the results of the stress distributions along the scratch profile and along the scratching direction.

2.4.3. Scratch profile evaluation

The scratch profiles were obtained for both, experimental and simulated scratches. The experimental median profiles were extracted as part of the topographic measurements, while the profiles from simulations were extracted from the central section of each simulated scratch. This information was then post-processed using MATLAB [41] to quantify the scratch profile morphology via the abrasive wear factor according to Zum Gahr [42]

$$f_{ab} = \frac{A_v - (A_1 + A_2)}{A_v}, \tag{7}$$

where A_v is the area of the wear groove and A_1 and A_2 are the areas of the ridges deposited on the sides of the scratch. The terms used in Eq. (7) are illustrated in Fig. 4, based on this criterion, ideal cutting would result in a value of $f_{ab} = 1$, while ideal plowing would produce $f_{ab} = 0$ as no material is removed from the profile.

3. Results and discussion

3.1. Lattice sensitivity

A set of simulations was conducted in order to assess the influence of the particle size in the results of the simulations, analogous to a mesh sensitivity analysis in Finite Element Methods. The results should be consistent, and an optimal mesh/particle size has to be determined to properly capture the studied phenomena [43]. The goal is to obtain simulation results that are lattice independent while simultaneously optimizing the computational time.

Fig. 5 shows the results of the von Mises stress distribution for scratches with particle sizes of 10, 15 and 20 μm. While greater detail was observed with the 5 μm and 7.5 μm particle sizes (Fig. A.3), some numerical artifacts were observed in these results, which are a product of the finer domain decomposition required for the simulations with smaller particle sizes. This effect shows more critically in the central longitudinal cut of the scratch due to the distribution of computational domains along the y-axis. Care must therefore be taken how exactly the computational load is split between the processors, and the use of the optimal number of nodes is critical for minimizing the possible negative effects of the domain decomposition. For our system configuration, we found that the best setup to run the simulations would be using two nodes, with a total of 32 cores. This configuration minimized the communication times in the parallelization of the tasks. Other relevant parameters to take into account are the re-balancing settings, as well as the updating of neighbor lists and the communication style between processors.

Small particle sizes also under-represented the prescribed scratch depth, as shown in Fig. 6. However, for all cases the range of the stress distribution magnitude along the scratch remained within 0–2 GPa below the indenter tip, as can be observed in Fig. 5 without large variations.

The first row in Fig. 5 shows the corresponding stress distribution of the scratch profile while below the indenter. The second row depicts the residual stress distribution for the different particle sizes once the indenter has passed. Finally, the third row of snapshots shows the stress distribution along the scratch length for the different particle sizes with the indenter standing at the last position. Buzzi et al. [44] discussed the influence of space discretization of MPM simulations in 2D and found that there is a balance point between material points and grid nodes to achieve best accuracy with good efficiency.

The use of different particle sizes led to different morphologies of the scratch profiles generated in each simulation as shown in Fig. 6. Due to the interaction of the sample with the indenter as a rigid body, even if the indentation phase of the simulation is set to a fixed depth of 20 μm, the size of the particles had an influence on the response of the sample to the indenter, as well as the elastic rebound of the material. The quality assessment of the results was then based on the error of the obtained scratch profile for each simulation at a prescribed scratch depth and the resolution of the stress distribution over the scratch length.

The 10 μm particle size yielded a good compromise between the quality of the results and the required computational resources, as shown in Fig. A.4 where the simulation with the smallest particle size took up to 100 h versus the simulations with largest particles of 20 μm, which took 0.4 h for the same system. The solution of the simulation with the 10 μm particles was performed within a total time of 4.3 h for the jobs with a scratching speed of 50 m/s, which was a good compromise. All simulations were performed in an IBM iDataPlex Cluster consisting of 84 nodes with 16 processor cores and 64 GB RAM per node (total of 1344 cores and 5376 GB RAM); infiniband network with a total computing power of approx. 25 Tflops.

The 10 μm particle size has been used in the previous work of Varga et al. [23], Varga et al. [45] and Leroch et al. [24], where a consistently good correspondence between experiments and simulations was found alongside good quality of the results for a wide range of different materials. Vaucorbeil et al. [46] ran a similar exercise evaluating the convergence of the Total Lagrangian Material Point Method [47] simulations using cell sizes ranging from 25 to 10 μm and determining their best compromise with a 12.5 μm grid size when comparing the scratch profiles. In the study of Mishra et al. [48], the particle sizes investigated were 5, 10 and 15 μm, to finally run the simulations with the smallest particle size of 5 μm using an optimized mass scaling factor of 1e6 to reduce the computational cost. Contrary to a meshed system as in FEM, the particle size is not directly limiting the resolution as a mesh element in FEM. The particles are interconnected, which can be imagined as a system of springs, so they also interact with neighboring elements and much higher resolution of e.g. deformations can be achieved than a single particle's diameter.

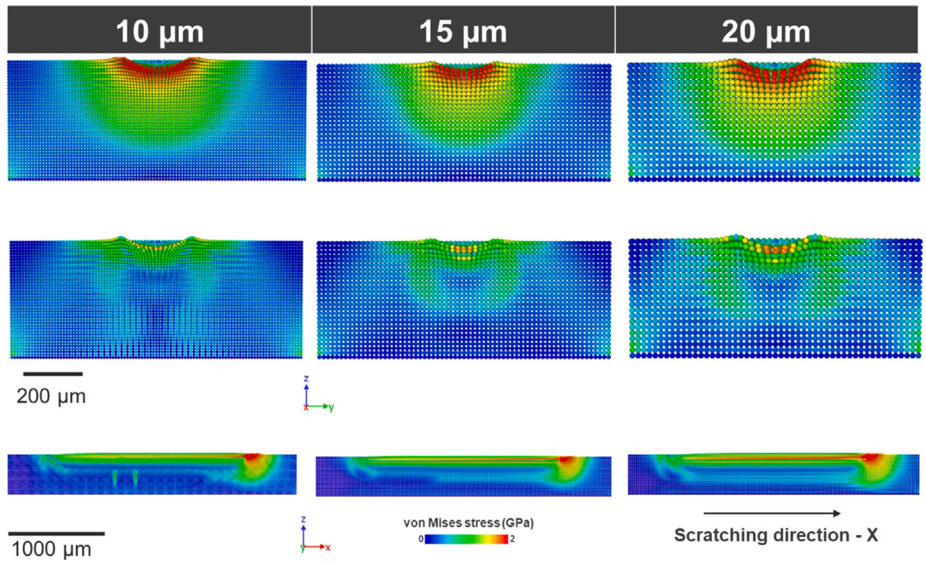

Fig. 5. Von Mises stress distribution of scratch profiles using different particle sizes. Results shown for 10, 15 and 20 μm particles. Scratching direction along the X axis.

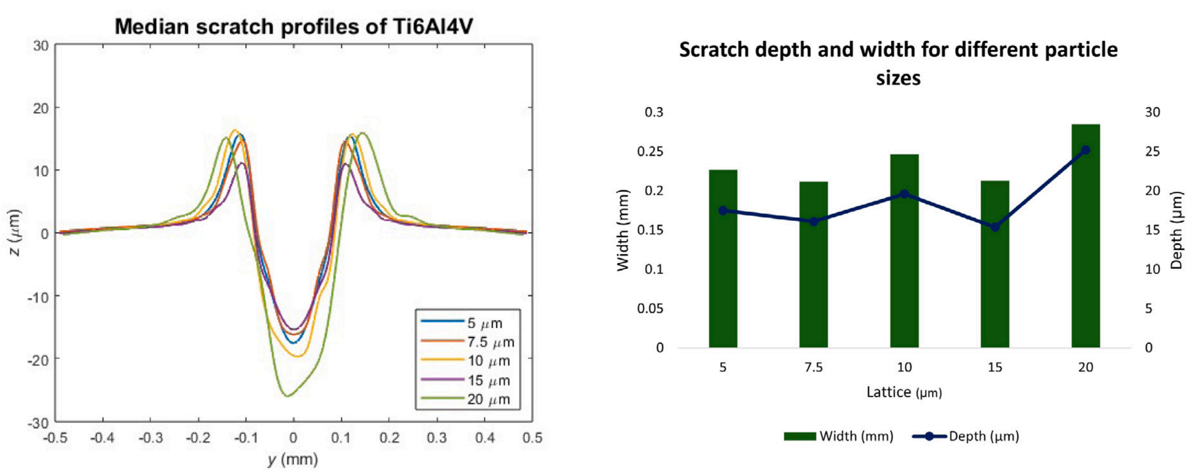

Fig. 6. Median scratch profiles for simulations with particle sizes of 5, 7.5, 10, 15, and 20 μm for a prescribed scratch depth of 20 μm and a scratch velocity of 50 m/s.

3.2. Scratch depths

This set of scratches was prepared to assess the correspondence between experimental and simulated scratches at different depths, namely 10, 20, and 25 μm. This was done to evaluate the overall response of the material when performing scratches at various depths comparable to experimental ones performed in the high-speed scratch set-up described in Section 2.2.

The results from experiments and simulations are shown in Fig. 7, from which the central part was further processed to obtain the mean profiles displayed in Fig. 8. We observed that while the depths of the scratches can be set very closely, the overall morphology of the scratch profiles is different, most notably the ridges formed on both sides of the scratched grooves. The median simulation scratch profiles exhibited higher ridges than their experimental counterparts. By contrast, the width of the scratch would be underestimated, on average, by 11.4% across the various depths in the simulations, and the depth would have an average error of 5.5% when comparing the experimental and simulation results. This difference between the scratch profiles from simulations and experiments was the first indication of a strain rate effect and its influence on the material response, as deeper scratches also lead (at the same scratch velocity) to higher strain rates. The simulated scratches shown in Fig. 8 were produced at a scratching speed of 100 m/s, while the experimental scratches were obtained at 6.5 m/s. The difference in scratching speed will consequently have an influence in the response of the material. This becomes more grave as the depth of the scratch increases and the difference between the experimental and simulated ridges is greater. Therefore, simulations at a comparable speed were deemed necessary. However, a clear correspondence was found when evaluating the abrasive wear factor for both, experimental and simulated scratches as shown in Fig. A.5. It can be observed how both sets of results exhibit the same trend with only

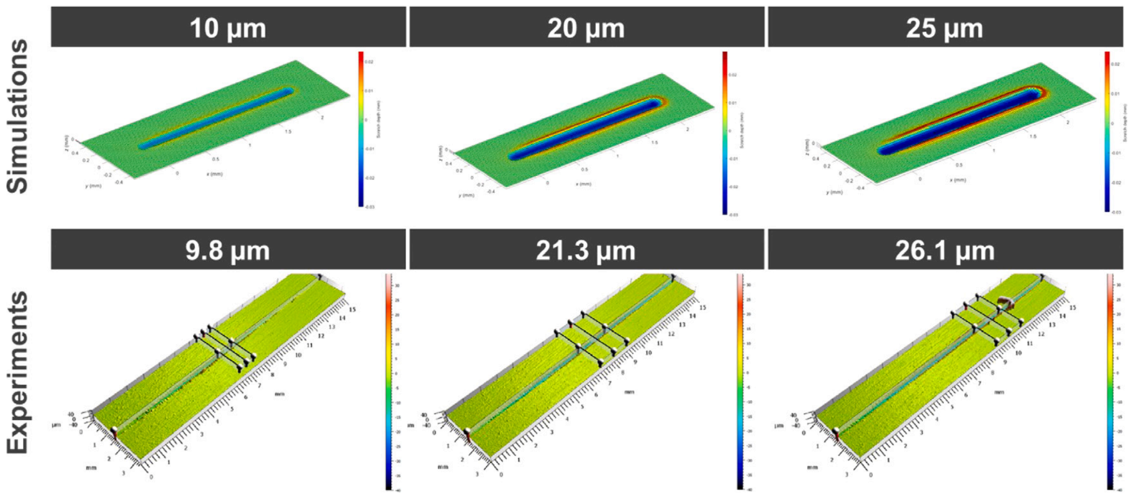

Fig. 7. Experimental and simulation results for scratches performed at various depths. Simulation scratch depths: 10, 20, and 25 μm at 100 m/s. Experimental depths of high-speed scratches (6.5 m/s): 9.8, 21.3, and 26.1 μm.

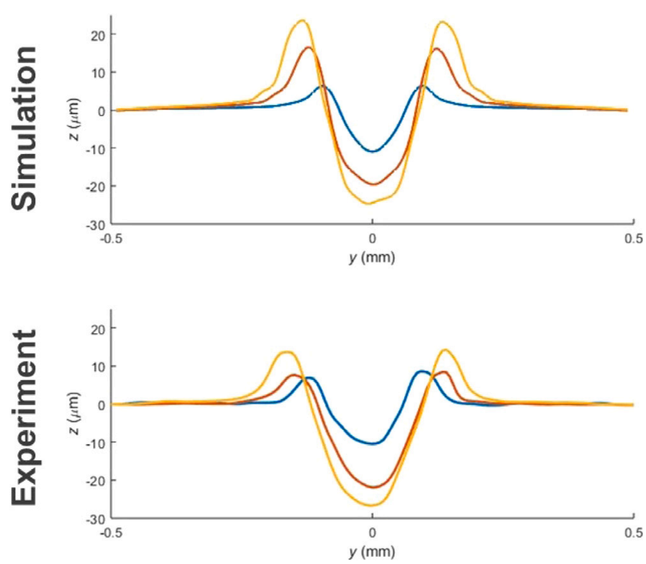

Fig. 8. Mean scratch profiles for simulated (100 m/s) and experimental scratches (6.5 m/s) at various depths: 10, 20, and 25 μm.

a slight offset between them. We interpret this trend as evidence of the correlation between experimental and simulation results, as the change with increasing depth between cutting and plowing is similar in both cases.

3.3. Scratch velocity

To comprehensively analyze the strain rate sensitivity of Ti6Al4V, a series of simulations was conducted at varying velocities, specifically at 100, 50, 10, 6.5, 5, and 1 m/s. These simulations were complemented by experimental scratch tests conducted under both, low and high-speed conditions, namely 5 mm/s and 6.5 m/s. The contrast of these results provide insights into the strain rate dependence of the material and may serve as future tool for determining the strain rate material parameters of metals by using high velocity scratch tests.

The results of the simulations in terms of stress distributions are shown in Fig. 9. As above, the first row shows a cross-section during scratching directly under the indenter, while the second row shows the residual stresses after the indenter has passed. For each scratching speed the stress distribution is different: while for the 10 m/s scratch the maximum stress below the indenter was 2.19 GPa, for its counterpart at 100 m/s it had an increased value of 2.35 GPa. Similarly, the residual stresses after the indenter has passed in the 10 m/s sample would reach a value of 1.37 GPa, while in the 100 m/s sample the stresses would remain at 1.56 GPa after indentation, as illustrated in Fig. 10 for each of the scratch speeds. When observing the entire range of scratch speeds, a logarithmic trend can be identified. The higher scratch speed is directly linked with a higher strain rate and corresponding increased strain hardening of the material. These insights provided by the simulation work are consistent with the response found by Lee et al. [13], where it was shown how the flow stress, material constants, and strain hardening are sensitive to the strain rate.

Additionally to the maximum stress values, also the stress distribution varies with the scratch speed. For the high speeds, the stresses are more localized below the wear track, also reaching higher maximum values as described above. The low-speed results show a wider distribution of medium stresses below the indenter (green area, ~1 GPa), which also leads to a wider extent of lower residual stresses, especially in the range of ~500 MPa. On the experimental level, corresponding behavior could be proven with EBSD measurements on aluminum in [20], where the cross-sections of scratches performed at various speeds were analyzed. Evaluations of the region directly below the surface were made by means of inverse pole figure (IPS) plots and grain average misorientation of the first 50 μm of depth, highlighting the evolution of the near surface region in different speed regimes.

Increased strain hardening also shows in the forces necessary for scratching. Our meshless simulations prove the overall increase in the forces required to scratch the sample as the scratch speed increases as depicted in Fig. 11, indicating the response and strain dependence of the material. The apparent coefficient of friction shown in Fig. A.6 is the ratio of tangential and normal forces during the scratch and provides a quantity to measure the resistance against deformation of the material. A small increase in the apparent coefficient of friction can be observed when increasing the scratching velocity. For the 10 m/s scratch the average COF is 0.287, while for the 100 m/s scratch is 0.297, this

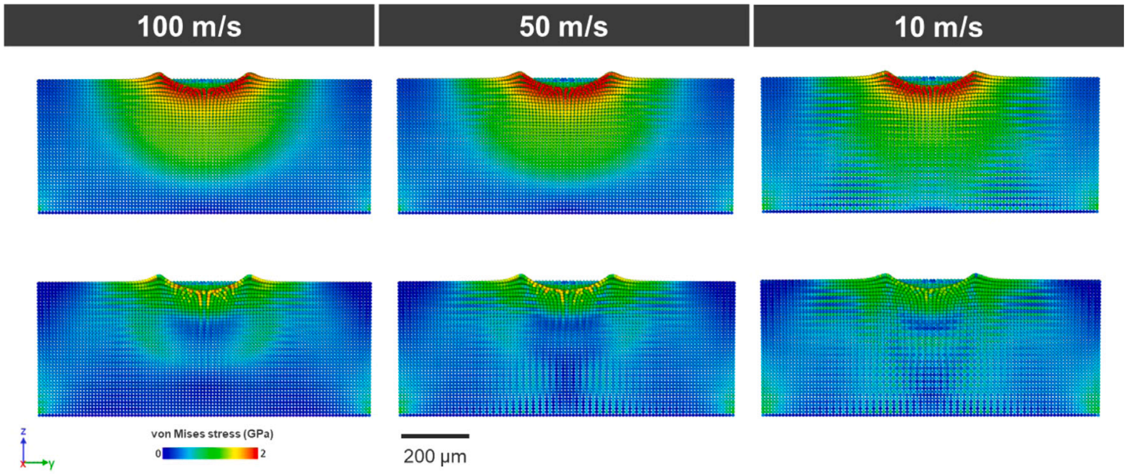

Fig. 9. Von Mises stress distribution of scratch profiles generated at various scratch speeds: 100, 50, and 10 m/s.

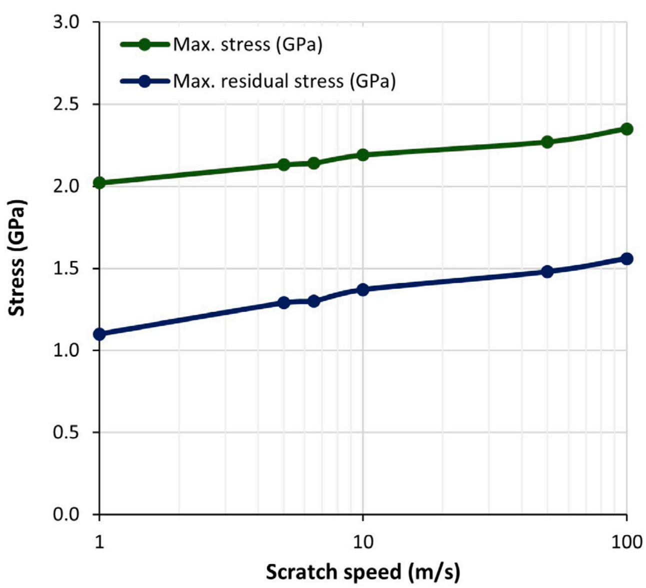

Fig. 10. Maximum stress below the indenter and maximum residual stress vs. scratch speed for simulations at 100, 50, 10, 6.5, 5, and 1 m/s.

slight increase reflects the increase in the scratching forces and brings evidence of the strain hardening behavior of the material.

The morphology of the median scratch profile also changes depending on the speed regime of the scratch. In Fig. 12(a), we present the evolution of the shape of the median scratch profiles in greater detail. The low-speed scratches (1 and 10 m/s) feature the formation of lower ridges with a height of ~2.6 μm, while the high-speed scratches exhibit the formation of higher ridges that reach heights up to ~7.75 μm. This behavior is consistent with that found experimentally as well as with the findings from previous investigations [23].

We associate the increasing trend in ridge height with two primary factors: the strain rate sensitivity of the material and its dynamic response under high-speed conditions. At higher scratching speeds, the material undergoes deformation at much higher strain rates. Titanium alloys like Ti6Al4V are known to be highly strain rate sensitive: as the strain rate increases, so does the flow stress. The Johnson–Cook model captures this behavior with a logarithmic term that increases the material's yield strength as the strain rate rises. As a result, during high-speed scratching, the material exhibits greater resistance to deformation, leading to a stiffer response, which has also been found experimentally [49].

The dynamic response of the material under high-speed scratching plays a relevant role in the formation of higher ridges. At high speeds, the effect of inertia become significant: the rapid motion of the indenter relative to the material introduces inertial forces that resist the immediate plastic flow. We believe that this resistance may limit the vertical displacement of the material into the groove, forcing more material to move sideways. Thus, the energy input during high-speed scratching is more likely to be dissipated through lateral flow and surface deformation rather than through deeper penetration and bulk plastic deformation, leading to the observed increase in ridge height. This interplay between strain rate sensitivity and dynamic response underlies the significant morphological differences in the scratch profiles at varying speeds, as seen in the evolution of the ridge heights from low to high-speed regimes.

The strain rate dependence response of Ti6Al4V described in the MPM simulations was also validated with the findings from experimental scratches by comparing scratches from the two speed regimes: a low-speed scratch performed at 5 mm/s and a high-speed scratch performed at 6.5 m/s. Fig. 12(b) shows the considerable difference in the ridge formation between the two samples, where the ridges from the high-speed scratch are ~5 μm higher on average than the ridges formed in the slow-speed scratch. This was the expected behavior that was also successfully captured in the simulations by making use of the strain hardening and strain rate sensitivity terms of the Johnson–Cook material model with parameters that were fitted to describe the response of the material at high strain rates.

Fig. 12(c) shows the good correspondence between the experimental and simulated scratches performed at ~6.5 m/s. The gray range of the simulated scratch profile is the range of scratch profiles obtained from the central region of the scratch length. Given that from the central millimeter various scratch profiles were extracted to get the median scratch profile of each simulation. Therefore, this gray range illustrates the range within which particles have displaced at different points in the central portion of the scratch. While the experimental scratch profile is the one extracted from the middle region of the scratch.

This comparison of both scratch profiles provides the ground for validation of the methodology to model the behavior of Ti6Al4V under

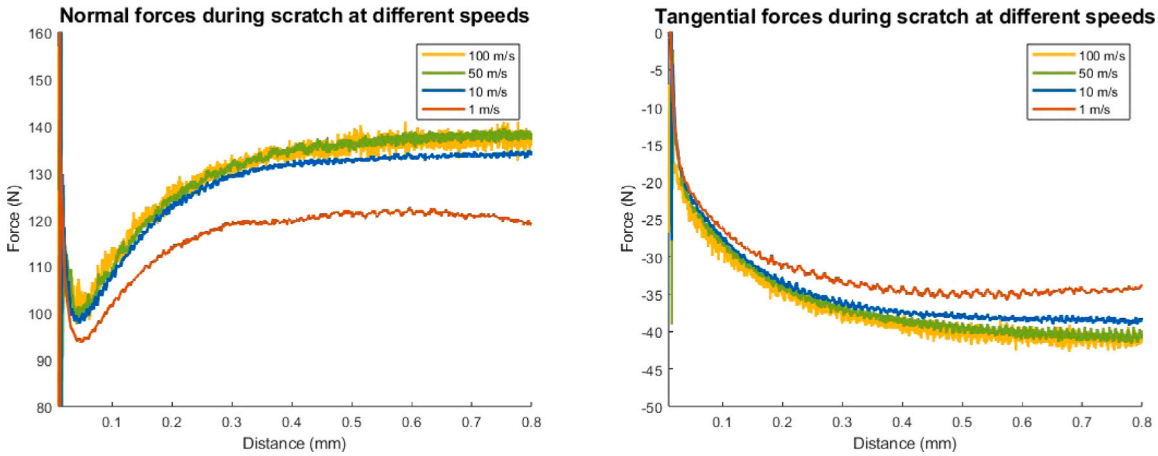

Fig. 11. Normal and tangential forces during scratch simulations at different speeds: 100, 50, 10 and 1 m/s.

abrasive load at high strain rates. The very good correlation at the overlapping speed allows us to infer that the behavior observed in the simulations at higher speeds, namely at 50 and 100 m/s, is a good representation of how the material would behave under such conditions. From these results, it should be highlighted that although the optimization of the Johnson–Cook parameters used for these simulations was validated using FEM simulations [33] and were not fitted or tailored in any way to MPM in the present work, this set of parameters was able to accurately represent the material behavior of the samples using our simulation technique. With this reliable and validated model for the Ti6Al4V behavior, the simulations are able to provide greater detail on the material response and strain rate dependence over a wider range of speeds.

Given the good agreement between the experiments and simulations, these become a relevant tool for extracting detailed information about the high strain rate behavior of Ti6Al4V. This research facilitates the extension of MPM simulations to address machining process challenges of the material, particularly those related to its poor thermal conductivity and high friction coefficients in the contact. Material characterization at high strain rates remains a challenging field, both in cost and efficiency. High strain rate scratches emerge as a promising method for assessing material parameters before machining simulations, offering a simpler alternative to complex tests like the Hopkinson bar. The ultimate aim is to leverage such techniques for determining metal behavior, potentially replacing traditional uniaxial experiments and advancing the understanding of material properties under dynamic conditions.

4. Conclusions

This work investigated the wear behavior of Ti6Al4V at high strain rates by means of scratch tests at high and low speeds that were performed experimentally and numerically modeled with the Material Point Method. We explored the influence of the particle size used in the simulations, finding an optimal particle size of 10 μm for the investigated scratching that represents best the prescribed scratch depth when interacting with the rigid body of the indenter. The use of this particle size also allowed a good compromise with the required computational resources.

The response of Ti6Al4V was documented for a range of scratch speeds up to 100 m/s and validated with the experimental scratch profiles obtained at ~6.8 m/s with the aid of a high-speed scratch test rig. Good compliance was found between experimental and simulated scratches when modeling the response of Ti6Al4V at high strain rates.

Through the simulation work it was possible to gain insights into the stress distributions and formation of residual stresses due to the high strain rate loading. The strain rate also had a substantial influence on normal and tangential forces and on the height of the ridges formed. This is in line with the experimental findings about a general increase in yield strength and work hardening of the samples. In this work, we managed to overlap the strain rate ranges accessible to both experimental and simulation techniques, allowing to close the gap between them and providing a validation of the method to be expanded in future work.

CRediT authorship contribution statement

A.M. Ventura Cervellón: Writing – original draft, Visualization, Software, Methodology, Investigation, Formal analysis, Data curation. **M. Varga:** Writing – review & editing, Resources, Project administration, Methodology, Funding acquisition, Conceptualization. **M. Rodríguez Ripoll:** Writing – review & editing, Resources, Project administration, Funding acquisition, Conceptualization. **S.J. Eder:** Writing – review & editing, Supervision, Resources, Methodology, Conceptualization.

Declaration of competing interest

The authors declare that they have no known competing financial interests or personal relationships that could have appeared to influence the work reported in this paper.

Data availability

Data will be made available on request.

Acknowledgments

This work was funded by the “Austrian COMET-Program” (Projects K2 InTribology1, no. 872176 and InTribology2, no. 906860) via the Austrian Research Promotion Agency (FFG) and the Provinces of Niederösterreich and Vorarlberg, and was carried out at the “Excellence Center of Tribology” (AC2T research GmbH). Open access funding was provided by TU Wien.

Appendix A. Supplementary data

Supplementary material related to this article can be found online at https://doi.org/10.1016/j.wear.2024.205554.

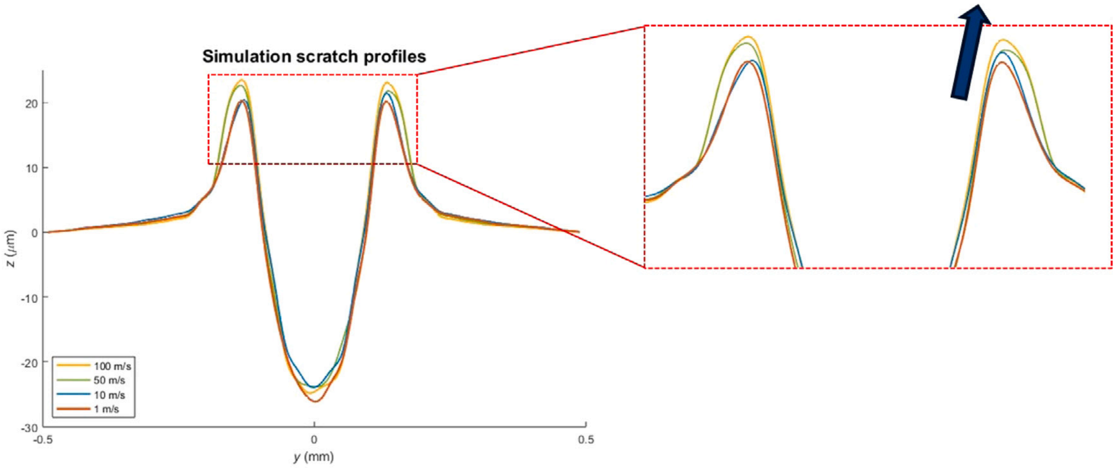

(a) Simulated mean scratch profiles generated at various scratch speeds: 100, 50, 10. and 1 m/s.

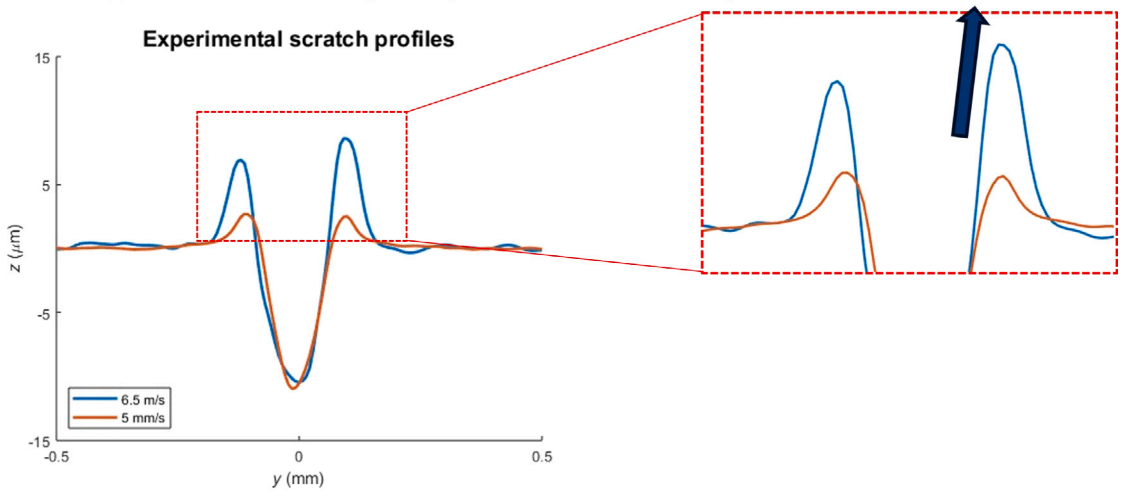

(b) Experimental mean scratch profiles generated at various scratch speeds: 6.5 m/s and 5 mm/s.

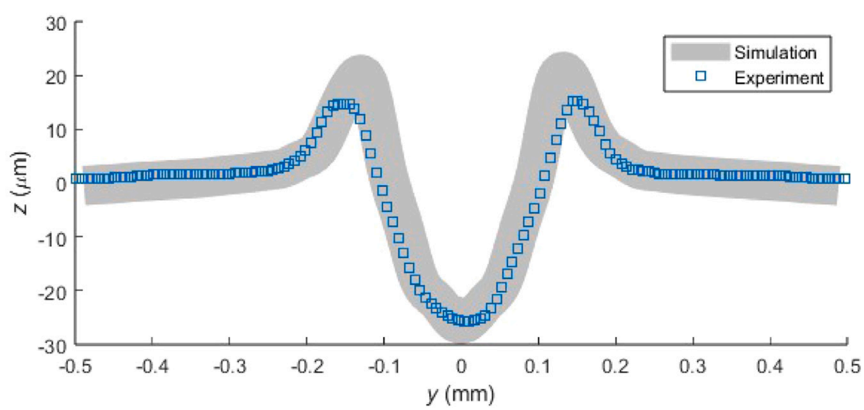

(c) Simulated mean scratch profiles generated at 6.5 m/s scratch speed.

Fig. 12. Simulated and experimental scratch profiles at various speeds.

References

[1] W. of Science, Web of science search on Titanium, 2024, URL: https://www.webofscience.com/wos/woscc/summary/2fc8421a-be2b-40d2-8b77-899328372f31-f4800b75/relevance/1.

[2] J.T. Philip, J. Mathew, B. Kuriachen, Tribology of Ti6Al4V: A review, Friction 7 (6) (2019) 497–536.

[3] M. Rahman, Z.-G. Wang, Y.-S. Wong, A review on high-speed machining of Titanium alloys, JSME Int. J. Ser. C 49 (1) (2006) 11–20.

[4] C. Leyens, M. Peters, Titanium and Titanium Alloys: Fundamentals and Applications, Wiley, Hoboken, 2006, OCLC: 990524473.

[5] C. Veiga, J. Davim, A. Loureiro, Properties and applications of titanium alloys: A brief review, Rev. Adv. Mater. Sci. 32 (2012) 133–148.

[6] H.-J. Choi, C.-W. Park, I.-S. Kang, J.-S. Kim, S.-D. Choi, Material model application considering strain softening for cutting simulation of Ti-6Al-4V alloy and its experimental validation, Int. J. Precis. Eng. Manuf. 17 (12) (2016) 1651–1658.

[7] K.G. Budinski, Tribological properties of titanium alloys, Wear 151 (2) (1991) 203–217.

[8] N. Joy, S. Prakash, A. Krishnamoorthy, A. Antony, Experimental investigation and analysis of drilling in Grade 5 Titanium alloy (Ti-6Al-4V), Mater. Today: Proc. 21 (2020) 335–339.
[9] H. Kolsky, An investigation of the mechanical properties of materials at very high rates of loading, Proc. Phys. Soc. B 62 (11) (1949) 676–700.
[10] H. Rojacz, M. Premauer, M. Varga, Alloying and strain hardening effects in abrasive contacts on iron based alloys, Wear 410–411 (2018) 173–180.
[11] S. Yadav, K.T. Ramesh, The mechanical properties of tungsten-based composites at very high strain rates, Mater. Sci. Eng. A 203 (1–2) (1995) 140–153, Publisher: Elsevier.
[12] C.Y. Chiem, J. Duffy, Strain rate history effects and observations of dislocation substructure in aluminum single crystals following dynamic deformation, Mater. Sci. Eng. 57 (2) (1983) 233–247.
[13] W.-S. Lee, C.-F. Lin, Plastic deformation and fracture behaviour of Ti–6Al–4V alloy loaded with high strain rate under various temperatures, Mater. Sci. Eng. A 241 (1–2) (1998) 48–59.
[14] G.G. Ye, S.F. Xue, W. Ma, L.H. Dai, Onset and evolution of discontinuously segmented chip flow in ultra-high-speed cutting Ti-6Al-4V, Int. J. Adv. Manuf. Technol. 88 (1) (2017) 1161–1174.
[15] M.K. Gupta, H.E. Etri, M.E. Korkmaz, N.S. Ross, G.M. Krolczyk, J. Gawlik, N. Yaşar, D.Y. Pimenov, Tribological and surface morphological characteristics of titanium alloys: a review, Arch. Civ. Mech. Eng. 22 (2) (2022) 72.
[16] S. Bellemare, M. Dao, S. Suresh, A new method for evaluating the plastic properties of materials through instrumented frictional sliding tests, Acta Mater. 58 (19) (2010) 6385–6392.
[17] P. Leroux, Scratch hardness measurement using mechanical tester, 2014, http://dx.doi.org/10.13140/RG.2.1.3120.0164.
[18] A.-T. Akono, N.X. Randall, F.-J. Ulm, Experimental determination of the fracture toughness via microscratch tests: Application to polymers, ceramics, and metals, J. Mater. Res. 27 (2) (2012) 485–493.
[19] A. Molinari, C. Musquar, G. Sutter, Adiabatic shear banding in high speed machining of Ti–6Al–4V: experiments and modeling, Int. J. Plast. 18 (4) (2002) 443–459.
[20] M. Varga, A.M. Ventura Cervellón, S. Leroch, S.J. Eder, H. Rojacz, M. Rodríguez Ripoll, Fundamental abrasive contact at high speeds: Scratch testing in experiment and simulation, Wear (2023) 204696.
[21] A.P. Thompson, H.M. Aktulga, R. Berger, D.S. Bolintineanu, W.M. Brown, P.S. Crozier, P.J. in 't Veld, A. Kohlmeyer, S.G. Moore, T.D. Nguyen, R. Shan, M.J. Stevens, J. Tranchida, C. Trott, S.J. Plimpton, LAMMPS - a flexible simulation tool for particle-based materials modeling at the atomic, meso, and continuum scales, Comput. Phys. Comm. 271 (2022) 108171.
[22] C. Jiang, C. Schroeder, J. Teran, A. Stomakhin, A. Selle, The material point method for simulating continuum materials, in: ACM SIGGRAPH 2016 Courses, SIGGRAPH '16, Association for Computing Machinery, New York, NY, USA, 2016, pp. 1–52, http://dx.doi.org/10.1145/2897826.2927348.
[23] M. Varga, S. Leroch, T. Gross, H. Rojacz, S. Eder, M. Grillenberger, M. Rodríguez Ripoll, Scratching aluminium alloys – Modelling and experimental assessment of damage as function of the strain rate, Wear 476 (2021) 203670.
[24] S. Leroch, S.J. Eder, M. Varga, M. Rodríguez Ripoll, Material point simulations as a basis for determining Johnson–Cook hardening parameters via instrumented scratch tests, Int. J. Solids Struct. 267 (2023) 112146.
[25] W. Shen, J. Sun, J. Liu, W. Mao, J.D. Nordstrom, P.D. Ziemer, F.N. Jones, Methods for studying the mechanical and tribological properties of hard and soft coatings with a nano-indenter, JCT Res. 1 (2) (2004) 117–125.
[26] J.L. Bucaille, E. Felder, G. Hochstetter, Mechanical analysis of the scratch test on elastic and perfectly plastic materials with the three-dimensional finite element modeling, Wear 249 (5) (2001) 422–432.
[27] D.A. Doman, R. Bauer, A. Warkentin, Experimentally validated finite element model of the rubbing and ploughing phases in scratch tests, Proc. Inst. Mech. Eng. B 223 (12) (2009) 1519–1527.
[28] K. Holmberg, A. Laukkanen, H. Ronkainen, K. Wallin, S. Varjus, J. Koskinen, Tribological contact analysis of a rigid ball sliding on a hard coated surface: Part II: Material deformations, influence of coating thickness and Young's modulus, Surf. Coat. Technol. 200 (12) (2006) 3810–3823.
[29] K. Holmberg, A. Laukkanen, H. Ronkainen, K. Wallin, S. Varjus, J. Koskinen, Tribological contact analysis of a rigid ball sliding on a hard coated surface: Part I: Modelling stresses and strains, Surf. Coat. Technol. 200 (12) (2006) 3793–3809.
[30] A. Laukkanen, K. Holmberg, J. Koskinen, H. Ronkainen, K. Wallin, S. Varjus, Tribological contact analysis of a rigid ball sliding on a hard coated surface, Part III: Fracture toughness calculation and influence of residual stresses, Surf. Coat. Technol. 200 (12) (2006) 3824–3844.
[31] B. Committee, Specification for Titanium and Titanium Alloy Strip, Sheet, and Plate, Technical Report, ASTM International, 2020, http://dx.doi.org/10.1520/B0265-20A, URL: http://www.astm.org/cgi-bin/resolver.cgi?B265-20A.
[32] M.A. Mekicha, M.B. de Rooij, T. Mishra, D.T.A. Matthews, L. Jacobs, D.J. Schipper, Study of wear particles formation at single asperity contact: An experimental and numerical approach, Wear 470–471 (2021) 203644.
[33] L. Xinjian, Y. Guigen, W. Zhimin, X. Shifeng, Z. Yi, Optimization on the Johnson-Cook parameters of Ti-6Al-4V used for high speed cutting simulation, J. Phys. Conf. Ser. 1653 (1) (2020) 012034.
[34] C..A. technical ceramics, DIN EN 1071-3:2005 - advanced technical ceramics - Methods of test for ceramic coatings - Part 3: Determination of adhesion and other mechanical failure modes by a scratch test, 2005, URL: https://webstore.ansi.org/standards/din/dinen10712005.
[35] Standard test method for scratch hardness of materials using a diamond stylus, 2009, URL: https://www.astm.org/g0171-03r17.html.
[36] D. Sulsky, Z. Chen, H.L. Schreyer, A particle method for history-dependent materials, Comput. Methods Appl. Mech. Engrg. 118 (1) (1994) 179–196.
[37] S. Bardenhagen, E. Kober, The generalized interpolation material point method, CMES Comput. Model. Eng. Sci. 5 (6) (1970) 477–496, Number: 6 Publisher: Tech Science Press.
[38] G.C. Ganzenmüller, Smooth mach dynamics - LAMMPS user guide, 2014.
[39] G.R. Johnson, W.H. Cook, Fracture characteristics of three metals subjected to various strains, strain rates, temperatures and pressures, Eng. Fract. Mech. 21 (1) (1985) 31–48.
[40] A. Stukowski, Visualization and analysis of atomistic simulation data with OVITO–the Open Visualization Tool, Modelling Simul. Mater. Sci. Eng. 18 (1) (2009) 015012.
[41] T.M. Inc., MATLAB, 2023, URL: https://www.mathworks.com.
[42] K.-H.Z. Gahr, Microstructure and Wear of Materials, Elsevier, 1987, Google-Books-ID: qibApT7zNcYC.
[43] L. Guo, J. Xiang, J.-P. Latham, B. Izzuddin, A numerical investigation of mesh sensitivity for a new three-dimensional fracture model within the combined finite-discrete element method, Eng. Fract. Mech. 151 (2016) 70–91.
[44] O. Buzzi, D.M. Pedroso, A. Giacomini, Caveats on the implementation of the generalized material point method, CMES Comput. Model. Eng. Sci. 31 (2) (2008) 85–106.
[45] M. Varga, S. Leroch, S.J. Eder, H. Rojacz, M.R. Ripoll, Influence of velocity on high-temperature fundamental abrasive contact: A numerical and experimental approach, Wear 426–427 (2019) 370–377.
[46] A. de Vaucorbeil, V.P. Nguyen, C.R. Hutchinson, M.R. Barnett, Total Lagrangian Material Point Method simulation of the scratching of high purity coppers, Int. J. Solids Struct. 239–240 (2022) 111432.
[47] A. de Vaucorbeil, V.P. Nguyen, C.R. Hutchinson, A total-Lagrangian Material Point Method for solid mechanics problems involving large deformations, Comput. Methods Appl. Mech. Engrg. 360 (2020) 112783.
[48] T. Mishra, G.C. Ganzenmüller, M. de Rooij, M. Shisode, J. Hazrati, D.J. Schipper, Modelling of ploughing in a single-asperity sliding contact using material point method, Wear 418–419 (2019) 180–190.
[49] R. Zhang, B. Wang, Z. Liu, L. Jiang, Y. Cai, Q. Song, Strain rate effect on material deformation and removal behavior during high speed scratching of 4H-SiC, Tribol. Int. 187 (2023) 108756.